RSC Advances

This article can be cited before page numbers have been issued, to do this please use: M. Pal, S. Bera and S. Jana, *RSC Adv.*, 2015, DOI: 10.1039/C5RA12322D.

ROYAL SOCIETY OF CHEMISTRY

www.rsc.org/advances

View Article Online
DOI: 10.1039/C5RA12322D

Sol-gel based simonkolleite nanopetals with SnO_2 nanoparticles in graphite-like amorphous carbon as efficient and reusable photocatalyst

Moumita Pal, Susanta Bera and Sunirmal Jana*

Sol-Gel Division
CSIR–Central Glass and Ceramic Research Institute (CSIR–CGCRI)
196 Raja S.C. Mullick Road, P.O. Jadavpur University, Kolkata 700032, India

Abstract

We report a new sol-gel nanocomposite (*STC*) having simonkolleite nanopetals (*SC*) and quasi-spherical tin oxide (*SO*) nanoparticles embedded in graphite-like amorphous carbon (*C*) as an efficient and reusable photocatalyst towards degradation of Rhodamine 6G (Rh 6G) dye under UV (λ, 254 nm) illumination. The *STC* was synthesized under vacuum curing (450^{o}C) of precursor gel derived from the sol (Zn : Sn, 2 : 1) in 2-methoxy ethanol with acetylacetone. Presence of tetragonal *SO* well decorated on rhombohedral *SC* forming nanoheterostructures in the carbon matrix was identified by X-ray diffraction, micro-Raman, X-ray photoelectron spectroscopy and electron microscopes (field emission scanning electron and transmission electron) studies. Carbon content and thermal weight loss behaviour in *STC* were studied by carbon determinator and thermogravimetry. The nanocomposite showed high photocatalytic activity (10^{-5}M dye solution degraded completely in 32 min). Reusability test of the photocatalyst exhibited about 95% of the dye degradation after five successive recycles. In addition to accelerate photo-induced charge carrier separation and electron transport in the nanoheterostructures as revealed from electrochemical impedance spectroscopy response of the UV exposed nanocomposite, an active role of the carbon in an optimum content (~18%) was found for generating high BET specific surface area (~143 m^2/g). This simple synthesis strategy could open a new avenue to develop sol-gel nanocomposites as efficient and reusable photocatalysts from simonkolleite based different metal oxide semiconductors embedded in graphite-like amorphous carbon.

Key words: Sol-gel process, simonkolleite, tin oxide, graphite-like amorphous carbon, nanoheterostructures, photocatalysts

***Corresponding author: Tel.: +91 33 23223303, Fax: +91 33 2473 0957
E-mail address: sjana@cgcri.res.in, janasunirmal@hotmail.com (S. Jana)

View Article Online
DOI: 10.1039/C5RA12322D

1. Introduction

Water pollution problem related to contamination of organic dyes is a serious global concern.[1] In this regard, the synthetic wastewaters from different dye industries have posed a great threat to the water environment.[2] The problem concerning the pollution could be mitigated cost effectively and economically by the use of nano metal oxide semiconductor (MOS) as photocatalyst under illumination of light.[3] However, the fast recombination of photogenerated electrons and holes (charge carriers) could diminish the photocatalytic activity of the MOS.[4] Thus, it is necessary to reduce the recombination rate of charge carrier that could enhance the lifetime of electrons and holes, resulting an improvement of the activity of semiconductors.[2] Accordingly, several strategies could be adopted. One could be an intentional creation of surface defects by incorporation of suitable doping element into the host crystal lattice.[5] The defects could act as trap states that reside within the band gap of MOS. This strategy could result in the reduction of recombination rate of charge carrier. In the same vein, the existence of nano heterostructures from mixed oxide semiconductors could also be regarded as an effective strategy.[3,6] These heterostructures could be constructed by different metal oxide semiconductors (such as ZnO, SnO_2, TiO_2) with wide band-gap energy.[6,7-9] Now-a-days, the nano heterostructures attracts the materials scientists due to their remarkable properties and several applications[10] including photocatalysis. With respect to the activity, the large specific surface areas as well as unique spatial architectures of the heterostructures could make them highly efficient photocatalysts. It could improve the efficiency of photocatalytic activity by reducing the recombination rate of photogenerated charge carrier and accelerates the reduction-oxidation reactions for degradation of organic pollutants (e.g. organic dyes).

It is worthy to note[11-13] that the carbon (e.g. graphene, carbon nano tube, amorphous carbon) could couple with several basic materials (such as oxides, metals, polymers) to

View Article Online
DOI: 10.1039/C5RA12322D

advance their functional properties including their optoelectronic property. Therefore, for enhancement of photocatalytic activity of a semiconductor, major works had already been reported on carbon (C) coupled single metal oxide semiconductor (such as ZnO/C, SnO_2/C, TiO_2/C) nanocomposites.[11-13] Also, very recently, carbon coupled mixed metal oxide semiconductors (e.g. α-Fe_2O_3/Mn_3O_4/graphene), which showed excellent charge transfer performance towards photocatalytic water oxidation had also been reported.[14] In the carbon-coupled nanocomposite, the photogenerated electrons would accumulate on the surface of carbon to convert O_2 to $O_2^{\bullet}$ and the holes could remain on the semiconductor surface transforming H_2O / ^{-}OH to $^{-}OH^{\bullet}$ for fast degradation of organics.[15] On the other hand, the carbon could enhance the textural property (particularly surface area and porosity) that could necessary for effective contact of photodegradable organic dyes.

Simonkolleite ($Zn_5(OH)_8Cl_2.H_2O$, SC) synthesized mostly by hydrothermal, sonochemical and sol-gel processes is known as common corrosion product for zinc bearing materials.[16,17] It can also enhance the performance of photoelectrochemical cells.[17] The SC could be transformed into ZnO by thermal heating at relatively lower temperatures.[16] Moreover, simonkolleite is now recognized as one of the wide band gap semiconductors having electronic band structure similar to ZnO (bulk band gap energy, 3.3 eV).[17] As a semiconductor, the SC could also be able to decompose organic dye (e.g. methyl orange). It is also known that the electrochemical/photochemical property of SC could improve by coupling with TiO_2.[18] This would form heterostructures, SC/TiO_2. On the other hand, SnO_2 is a well-known MOS having widespread applications (e.g. Li-ion batteries, gas sensing, photovoltaic conversion etc.).[11] However, the photocatalytic activity of SnO_2 is low.[19] To the best of our knowledge, no report is yet available on carbon coupled simonkolleite based heterostructure semiconductors nanocomposite that would act as carbon coupled mixed semiconductors. With this aspect, we considered SC/SnO_2 as a new heterostructure system. In addition, due to ability of

View Article Online
DOI: 10.1039/C5RA12322D

carbon to couple easily with several materials even with heterostructures, we attempted to synthesize in-situ a nanocomposite of carbon coupled SC/SnO_2 heterostructures. In this system, it could be expected that the photogenerated electrons of SC would transfer to SnO_2 as the electronic band structure of SC is similar to ZnO.[17] This would result the wide separation vis-à-vis reduction in recombination rate of charge carrier. Moreover, the carbon in the nanocomposite could further enhance the photogenerated charge separation in the photo-responsive materials through accelerating electron transport and improvement of the textural property that could be a favourable factor for enhancement of photocatalytic activity of the material towards degradation of organic dye under light illumination.[20] In this respect, we should mention that α-Fe_2O_3/Mn_3O_4/graphene composite has very recently been reported for photocatalytic water oxidation.[14] The reported work is a motivation of this work.

Sol-gel is a facile technique especially for preparation of thin films and nanomaterials. In this technique, the properties of a material (such as microstructural, optical, electronic, optoelectronic) primarily depend upon several parameters such as precursor composition and chemistry, doping etc.[5] Moreover, the curing treatments (e.g. vacuum curing, controlled-atmosphere curing) could also influence significantly upon the properties. This is because various chemisorptions and desorption processes and oxygen diffusion mechanisms are highly involved during the curing treatments.[5] However, among different curing treatments, the vacuum curing could found to be a very important one as carbon based nanocomposite sol-gel material for advanced applications could be developed from metal-organic precursor through the curing.[21]

Previously, we reported[8,9] the change of crystallinity, morphology and microstructure, optical and photocatalytic properties of vacuum cured ZnO-SnO_2 thin films on glass from the sols of varying Zn to Sn atomic ratio (1.86 : 1 to 2.33 : 1; *R*) / sol pH using zinc acetate dihydrate and tin chloride pentahydrate in 2-methoxy ethanol with acetylacetone as sol a

View Article Online
DOI: 10.1039/C5RA12322D

stabilizer. A detailed study[8] was also performed on sol to gel formation, chemical and physical properties of sols. However, adopting a particular synthesis process, the properties (like morphological, optical, photocatalytic etc.) of material in nano powder would differ from the nanostructured thin film.[22] Therefore, in the present work, the zinc-tin containing gel, derived from the precursor sol (Zn : Sn, 2 : 1) was cured systematically under the vacuum condition to obtain a nanocomposite powder. For the first time, in the nanocomposite, we found the formation of petal-like rhombohedral simonkolleite well decorated with tetragonal SnO_2 nanoparticles embedded in graphite-like amorphous carbon as confirmed by X-ray diffraction, micro-Raman, XPS, FESEM, TEM, etc. Moreover, the nanocomposite was mesoporous in nature, owning high specific surface area as studied by BET nitrogen adsorption-desorption isotherms. An excellent photocatalytic activity (PA) of the sample towards degradation of rhodamine 6G dye considered to be a water pollutant was observed under UV illumination (λ, 254 nm) (complete dye degradation in 32 min only). It is found that the presence of an optimum content (~18%) of carbon in the nanocomposite enhanced the photocatalytic activity over 6.5 times than simonkolleite/SnO_2 nano heterostructures. Reusability study up to five successive recycles showed excellent performance of the photocatalyst. In brief, this report discloses for the first time, a very simple strategy for the development of carbon-coupled simonkolleite/SnO_2 nanocomposite for efficient photocatalytic degradation of rhodamine 6G.

2. Experimentals

2.1 Precursor sols

In this work, all the chemicals were used as received without their further purifications. The precursor sol (ZSS) for simonkolleite-tin oxide-carbon nanocomposite material (ZSV) was made by using zinc acetate dihydrate (ZA, Sigma Aldrich, purity 98%; as a zinc source) and

View Article Online
DOI: 10.1039/C5RA12322D

stannic chloride pentahydrate (TCP, Loba Chemie, purity 99.5%; as a tin oxide source) in 2-methoxy ethanol (SRL, India, 99%) solvent having acetylacetone (acac) as sol stabilizing agent. In the precursor sol, the Zn to Sn (atomic ratio) was 2 : 1. The details of preparation of the sol and their properties had already been reported in our previous work.[8] However, in a brief preparation of sol, the required quantities of ZA and TCP were dissolved in 2-methoxy ethanol (SRL, 99%) with acetylacetone. A sol (SS) was also prepared using TCP in 2-methoxy ethanol in presence of acetylacetone. In addition, another sol (ZS′S) was also made using ZA and TCP in 2-methoxy ethanol without adding acetylacetone. Moreover, using zinc chloride (ZC, Sigma Aldrich, purity 98%; as Zn source) in 2-methoxy ethanol with acac, a different sol (Z′S) was also prepared. It is important to mention that the equivalent oxide weight percentage (wt.%) and the molar ratio of acac with ZA or TCP (in case of ZA free sol) were kept fixed at 4.0 wt.% and 1 : 1.4, respectively. Further, fixing oxide content (4%) and Zn to Sn molar ratio (2 : 1), two different sols were also prepared. These sols were named as ZSS-LC and ZSS-HC with molar ratio of acac to ZA, 1 : 1 and 1 : 2, respectively. Finally, the as-prepared transparent sols in Borosil glass beakers of 200/500 ml capacity were placed in a clean room (temperature, ~30^{o}C; relative humidity, 50-55%) to obtain gels from the precursor sols. It is noted that the TCP containing sols showed shorter gelling time than ZA or ZC based sols. This could relate to different rate of hydrolysis of the salts.[8,23]

2.2 Nanocomposites

All the gels (ZSG-LC, ZSG, ZSV-HC, ZS′G, ZG and SG**)** were cured under vacuum condition (-1 mBar pressure) at 450^{o}±5˚C in an electrical vacuum furnace[8] with a heating rate of 2˚C/min and a soaking period of 1 h at the maximum temperature. The vacuum curing was performed to generate carbon matrix[21] in the cured samples (discussed later). Under the vacuum condition, the cooling process was continued up to ~250^{o}C with a cooling rate of

View Article Online
DOI: 10.1039/C5RA12322D

2˚C/min. Then, the furnace was allowed to cool down automatically to room temperature (30^{o}±5˚C) under the vacuum condition. It is important to note that the ZS′G vacuum cured sample was further heat treated (rate, 2^{o}C/min) at 400^{o}C in pure oxygen gas (flow rate, 2 litre/min) atmosphere for 1 h at the maximum curing temperature to remove the carbon from the sample. The final samples derived from ZSG-LC, ZSG, ZSV-HC, ZS′G, ZG and SG gels were termed as ZSV-LC, ZSV, ZSV-HC, ZS′V, ZV and SV, respectively. Moreover, the ZSG gel was also cured in an air atmosphere at 450^{o}C for 1 h duration without vacuum. This air cured sample was designated as ZSA. More details about the samples are given in **Table S1 (ESI)**.

We had already reported in our previous study[8] on the formation of acetylacetonato complexes of metal ions (Zn^{2+}/Sn^{4+}) present in the sols. However, in this work, the FTIR spectral study (**Fig. S1 and Table S2, ESI**) of the precursor gels dried at 130±5^{o}C for 2 h in an air oven suggested that acetylacetone/solvent was present as organics, chemically interacted with metal ions in the gels. These organics in the gels after curing under vacuum condition could generate carbon matrix (**Table S3**). It is important to mention that the formation of different inorganic crystals (**Fig. S2**) was also observed under the vacuum condition depending upon the curing temperature. We proposed chemical equations (eqns. 1 to 7, **ESI**) based on systematic FTIR and Raman spectral as well as X-ray diffraction, electron microscopes (field emission scanning electron and transmission electron) and X-ray photoelectron spectroscopy analyses (discussed in the later sections) for in-situ generated different products (especially simonkolleite, zinc oxychloride, tin oxide, zinc oxide and graphite-like amorphous carbon) derived from zinc-tin containing 130^{o}C dried gels, cured at different conditions (vacuum/oxygen/air**)** and temperature**s.**

View Article Online
DOI: 10.1039/C5RA12322D

2. Characterizations

2.1 Materials characterizations

In ZSV sample, the presence of crystalline phases were identified by X-ray diffraction (XRD) study employing an X-ray diffractometer (Philips PW 1730 XRD unit) with nickel-filtered CuK_α radiation source (wavelength, 1.5418 Å) in the diffraction angle (2θ), 10^o to 70^o. Morphology and microstructure of the samples were analyzed by field emission scanning electron microscope (FESEM and FESEM-EDS, ZEISS, SUPRA^{TM} 35VP). Transmission electron microscope (TEM) was employed to determine the particle shape and size, tentative metal content as well as crystalline phases of the samples using Tecnai G^2 30ST (FEI) electron microscope operating at 300 kV. Initially, the samples were dispersed in low boiling alcohol (such as ethanol) by ultrasonication for about 2 h and the dispersed samples were placed carefully onto the carbon coated Cu-grid (300 mesh). Simultaneous thermogravimetry, thermogravimetric–differential scanning calorimetry (TG-DSC) (NETZSCH STA 449F3 STA449F3A-0584-M) was carried out for ZSV to determine the weight loss behaviour of the sample in air up to 1050^oC using alumina as reference. Carbon content in the samples was analyzed by carbon determinator (LECO make, USA; Model C600). The rate of heating was maintained at 5.0 K/min during the TG-DSC run. Raman spectra (frequency range, 2000 – 200 cm^{-1}) of the composites were measured at room temperature by employing a micro-Raman spectrometer (Renishaw inVia Raman microscope) using an argon ion laser with the incident wavelength of 514 nm as an excitation source. The presence of different elements and their chemical states in the representative ZSV sample was determined by employing an X-ray photoelectron spectrometer (XPS) in the energy range, 200 – 1200 eV (PHI Versaprobe II Scanning XPS microprobe surface analysis system) using Al-K_α X-rays ($h\nu$, 1486.6 eV; ΔE, 0.7 eV at room temperature). The pressure in the XPS analysis chamber was better than $5x10^{-10}$ mbar and the energy scale of the spectrometer was calibrated with pure

View Article Online
DOI: 10.1039/C5RA12322D

Ag. Moreover, the position of C1s peak was taken as standard (binding energy, 284.5 eV). The specific surface area and pore size of the samples were measured by BET nitrogen adsorption and desorption isotherms studies at liquid nitrogen temperature by adopting a Quantachrome (Autosorb1) machine. All the samples were out gassed in the vacuum at suitable temperature for about 4 h prior to the measurement. Electrochemical impedance spectra (EIS) (Nyquist plots) of the samples (ZSV, ZS$^{/}$V, ZSA, ZV and SV) under UV light (λ, 254 nm in a custom built stainless steel UV curing chamber; details given in the next section) were recorded in the frequency range, 1-1000 kHz with an AC amplitude of 200 mV utilizing Metrohm make Autolab 3200N instrument. A fixed weight (5 mg) of a sample (photocatalyst) was added into 2 ml of 2-methoxy ethanol (SRL, India, 99%) and then, the aliquot was grinded initially for more than 10 min till a viscous paste was formed. Finally, the paste was deposited (area, 1 cm^2) onto a FTO glass (Technistro; sheet resistance, 10 Ω/□) adopting doctor blading technique. The deposited film electrode (area, 1 cm^2) was served as the working electrode. On the other hand, the platinum wire as counter electrode (CE) and the Ag/AgCl/3(M) KCl as reference electrode were also used in this measurement. Moreover, aqueous Na_2SO_4 (0.01M) solution prepared by using sodium sulphate salt (Ranbaxy, India, 99%) and deionized water from Milli-Q (Millipore, 18 MΩ) was used as the electrolyte solution.

2.2 Measurement of photocatalytic activity

Photocatalytic activity (PA) of the samples towards decomposition of rhodamine 6G (Rh6G) dye with an initial dye concentration of 10^{-5} (M) (C_o) in double distilled water was examined under UV (wavelength, 254 nm) in a custom built stainless steel UV curing chamber well equipped with a lid and an arrangement of three equally spaced UV lamps (power, 8 watt each). In each sample, a suspension was prepared by adding 50 mg of the catalyst into a 100

View Article Online
DOI: 10.1039/C5RA12322D

ml aqueous dye solution in the dark. In a specific time interval, ~ 4 ml of the dye solution was taken out from the photocatalytic reaction vessel (150 ml Borosil glass beaker) exposed under the UV light and separated the solid catalyst from the solution by centrifugation.[5] After that the visible absorption spectrum of the solution was recorded to find out the remnant dye concentration (C) with the help of a calibration curve of the dye solutions. The calibration curve was constructed by plotting dye concentration against absorbance (OD) at 527 nm peak wavelength of the solutions obeying Lambert-Bayer's law. The PA of the samples was analyzed by plotting *ln* (C_o/C) (dye concentration; C_o, initial and C, remnant) versus illumination time. The rate constants of decomposition reaction (considering first order reaction kinetics) were found out from the plots. All the details on the PA had already been reported elsewhere.[5,8] It is noted that PA activity of the representative ZSV sample was also carried out using specific chemicals (such as tert-butyl alcohol, potassium iodide, 1, 4-benzoquinone) in the dye solution for understanding the possible mechanism governing the PA. Moreover, to ensure the applicability as recycled photocatalyst, the reusability study of the ZSV photocatalyst up to five successive recycles was performed (**Fig. S3 and Tables S4, S5; ESI**). After 1st cycle, the catalyst was extracted by centrifugation and then washed thoroughly in de-ionized water. Subsequently, the recovered solid mass was washed with ethanol followed by drying it at 80^{o}C for about 5 h in an air even. The process was mimicked up to five successive recycles. The reusability study for the catalyst showed that there is a minor decrease (about 5%) in the dye decomposition (**Table S5, ESI**) after 5th successive recycles.

View Article Online
DOI: 10.1039/C5RA12322D

3. Results and discussion

3.1 Phase structure

Figure 1 shows the X-ray diffraction (XRD) patterns of ZSV including ZS′V, ZV and SV samples. All the samples were found to be nanocrystalline in nature (**Table S6, ESI**) as confirmed from the measurement of crystallite sizes from the XRD patterns of the samples using Scherrer's equation.[24] In ZSV, the XRD patterns (in terms of 2θ peaks) are fully matched with two different types of crystals; rhombohedral simonkolleite [r-SC, JCPDS Card 07-0155 and tetragonal SnO_2 [t-SnO_2, JCPDS Card 41-1445]. However, no trace of hexagonal ZnO (h-ZnO) was detected in the ZSV while in ZV both the presence of r-SC and h-ZnO was identified (**inset, Fig. 1**). It is interesting to note that in zinc-tin containing precursor gels (ZSG or ZS′G), the formation and stability of r-SC greatly depend upon the gel curing temperate (*T*) and atmosphere. However, the change of curing condition, did not affect the formation of t-SnO_2. It was also seen that under vacuum curing of ZSG precursor gel at 400^{o}C, the r-SC started to form (**Fig. S2, ESI**) but at the curing temperature of 450^{o}C, the sample was enriched with r-SC in addition to t-SnO_2. Any how, on further increasing the *T* to 500^{o}C, the XRD patterns of simonkolleite disappeared and several new peaks were noticed distinctly. It is noted that the peaks were fully matched with h-ZnO [JCPDS Card 36-1451]. On the other hand, the ZSG gel when cured at 450^{o}C under an air atmosphere, orthorhombic zinc oxychloride (o-ZnO.$ZnCl_2$.H_2O, o-ZOC) [JCPDS Card 45-0819] along with t-SnO_2 was identified but no trace of r-SC was found from the XRD patterns of ZSA sample. Moreover, the ZS′V sample prepared by two steps curing of ZS′G gel derived from ZSS equivalent sol compostion without adding acetylacetone was also showed the formation of o-ZOC with the presence of noticiable amount of r-SC. Here, the two steps curing means, the ZS′G gel initially cured under vacuum at 450^{o}C and further cured the sample at 300^{o}C in pure oxygen gas atmosphere for 2 h for removal of carbon (discussed details later under Raman spectral study, **Fig. 2**). Hence, the XRD study revealed that during thermal curing of zinc-tin

View Article Online
DOI: 10.1039/C5RA12322D

containing precursor gels (ZSG/ZS$^{/}$G), the air/oxygen atmosphere is not suitable for the formation of r-SC and most favourable condition for r-SC formation was the vacuum curing at the 450^{o}C temperature. On the other hand, the ZV and SV composites showed the presence of r-SC with small content of hexagonal ZnO and t-SnO_2, respectively as evident from their XRD patterns (**Fig. 1**). As reported by many authors[17,18,25-27], the formation of r-SC mainly depends on precursor sol/solution pH and temperature in rather complicated processes including hydrothermal, co-precipation and electrochemical etc. In this respect, the present preparation method of r-SC could certainly be a novel process. However, the exact role of vacuum curing on the formation of r-SC was yet to be investigated. Further, the FTIR spectral study (**Fig. S1, Table S2**) evidenced that the organics are present in the precursor gels even after the thermal baking at 130^{o}C. This could be an obvious observation of sol-gel process.[28] Moreover, under vacuum curing the gels, the formation of amorphous/crystalline carbon[21,29,30] could be expected in the sample (discussed deails later under Raman, XPS and TEM analyses). However, no characteristic XRD patterns for crystalline carbon were identified in the vacuum cured samples. This would indicate the formation of amorphous carbon, otherwise if the generated carbon is crystalline, its characteristic peaks would be disguised with the XRD peaks of t-SnO_2 / r-SC crystals**.** Sometimes, due to high dispersion[14] of carbon, the sample would not respond XRD also.

3.2 Raman spectra

Raman spectral study is an efficient tool for characterization of carbon materials.[31-35] Two distinct Raman peaks located at ~1595 cm^{-1} and ~1355 cm^{-1}, assigned to 'G' (graphene) and 'D' (defect) of carbon[14,31-35] were observed from the spectra of ZSV, ZV and SV (**Fig. 2**) as well as ZSV-LC and ZSV-HC (Fig. S4) samples prepared by curing the precusor gels under vacuum at 450^{o}C. However, when the gels were cured in air or pure oxygen atmosphere (in

View Article Online
DOI: 10.1039/C5RA12322D

the case of ZS/V and ZSA samples), the Raman vibrations were not found. It is important to note that the ZS/V sample was prepared by two steps curing process (initially cured under vacuum at 450^{o}C and finally, cured it again at 300^{o}C in pure oxygen gas atmosphere for 2 h) from ZS/G gel derived from ZSS equivalent sol compostion without adding acetylacetone. Also, the Raman spectrum (**inset, Fig. 2**) of 450^{o}C vacuum cured ZS/V sample showed the presence of carbon as evident from the observation of Raman peaks at ~1595 cm^{-1} and ~1355 cm^{-1}, corresponds to 'G' and 'D' of carbon. Generally, the G band represents the vibration of sp^2C in graphitic[32] domain while the D band demonstrates the sp^3C or disordered canbon structure.[14,33] In the present work, the appeared G band position is relatively higher than graphene.[32] It is known that the G band positon would depend upon the sp^3C/sp^2C fraction in carbon material.[34] With increasing the fraction of sp^3C, the in-plane co-relation length of graphitic layers would reduce which consequences the average G band position to move towards higher energy region.[35] This might be caused due to the shortening of interplanar distance, d_{002}[29] (discussed under TEM analysis, **Fig. 5**). Therefore, the Raman spectral analysis suggested that the present carbon in the vacuum cured samples could be graphite-like amorphous carbon. This amorphous carbon in simonkolleite-SnO_2 composite could be useful for improving photocatalytic activity towards degradation of organic dye[36] (discussed later). On the other hand, we measured the content of carbon in ZSV-LC, ZSV, ZSV-HC, ZV and SV samples by carbon determinator and the content of measured carbon was ~10%, ~18%, ~23.5%, ~6.5% and ~17%, respectively (**Table S3, ESI**). The lowest content of carbon in ZV could be a non-formation of zinc-acetylacetonato complex in the precursor gel drived from the sol using $ZnCl_2$ as zinc source. This was verified by FTIR spectra (**Fig. S1 and Table S2, ESI**) of 130^{o}C baked ZG gel.

View Article Online
DOI: 10.1039/C5RA12322D

3.3 XPS analysis

In ZSV sample, the presence of simonkolleite and SnO_2 semiconductors along with graphite-like amorphous carbon was evidenced from XRD (**Fig. 1**) structural and Raman spectral (**Fig. 2**) analyses. Mainly two different hybridizations, sp^2C and sp^3C could be expected in amorphous carbon.[32] However, the determination of relative content of sp^2C and sp^3C in the carbon could not possible from Raman study (**Fig. 2**). Therefore, XPS analysis (**Fig. 3)** of the sample was absolutely necessary to know the relative content of specific carbon. In addition, the presence of different elements with their chemical states was also essential for the purpose of Raman study. The existence of non-metallic elements such as carbon, chlorine and oxygen as well as metallic elements such as zinc and tin were identified from their corresponding binding energy signals in the XPS survey spectrum (**Fig. 3a**) of the sample. The sources of carbon, chlorine and oxygen could be the graphite-like amorphous carbon, simonkolleite and simonkolleite-SnO_2, respectively as evident from Raman (**Fig. 2**) and XRD (**Fig. 1**) studies of the sample. In case of the carbon, a broad asymmetrical signal of C1s core level could be decomposed into two Gaussian fitted components with the binding energy peaks, located at 284.1±0.1 eV and 285.9±0.2 eV, assigned to sp^2C and sp^3C carbons, respectively (**Fig. 3b**). Form the peak area of the signals, the calculated relative contents of the sp^2C and sp^3C carbons are ~55.5% and ~44.5%, respectively. Thus, the XPS data strongly supported the Raman spectral study (**Fig. 2**) related to the existence of graphite-like amorphous carbon.[35] Another broad signal was appeared with the peak energy of ~530 eV for O1s that could split into Gaussian-fitted two distinct peaks (**Fig. 3c**) located at 530.1±0.1 eV (S1) and 531.6 ±0.2 eV (S2). The values of peaks for O1s matched with the reported data by Chen et al.[37] However, the S1 signal could relate to O^{2-} ions[37]of simonkolleite and SnO_2 as evident from XRD (**Fig. 1**) and Raman spectra (**Fig. 2**) while the S2 signal could assign to O^{2-} ions of oxygen deficient semiconductors (simonkolleite, SnO_2).[5] On the other hand, the

View Article Online
DOI: 10.1039/C5RA12322D

binding energy peaks of (**Fig. 3d**) $Zn2p_{1/2}$ and $Zn2p_{3/2}$ core levels were observed at 1044.8±0.2 eV and 1021.7±0.1 eV, respectively. The energy difference between the two core levels is 23.1±0.1 eV, matched well with the reported value for Zn^{2+}.[5,38] On the other hand, the XPS spectrum of the sample showed triplet signals of Sn3d (**Fig. 3e**). The triplet signals with decreased peak intensity were appeared at 486.4±0.2, 494.9 ±0.1 and 499.3±0.2 eV, could be originated from the core levels of $Sn3d_{5/2}$, $Sn3d_{3/2}$ and $Sn3d_{1/2}$, respectively.[38,39] However, the binding energy difference of $Sn3d_{5/2}$ and $Sn3d_{3/2}$ core levels is 8.4 eV (Δ). In this respect, Shi et al[38] also reported a similar value of Δ. It is known that in $Sn3d_{5/2}$, the binding energies of Sn^{4+} (486.5 eV) and Sn^{2+} (486.25 eV) are very close[40]. Therefore, it is difficult to separate Sn^{2+} from Sn^{4+} from the XPS data. However, the presence of tetragonal SnO_2 from XRD pattern (**Fig. 1**) of the sample could emphasize on the existence Sn^{4+}. Further, the XPS signal for Sn^{o} could appear at relatively low energy (484.6 eV)[41] compare to the energy of the signal for Sn^{4+}/Sn^{2+}. In fact, it was not detected from the XPS measurement. Hence, the possibility of Sn^{o} formation could be discarded in the sample.

3.4 Morphology and microstructure

3.4.1 FESEM study

Figures 4 and S5 **(ESI)** display the FESEM results of ZSV, ZV and ZSA along with ZS′V and SV samples. The FESEM images (**Fig. 4a,i**) of ZSV sample clealry shows the particles with petal-like hierarchical structures (petal thickness, 28-41 nm; inset, **Fig. 4i**) together with quasi-spherical particles (average size, 15±3 nm) embedded in a featureless matrix (**inset, Fig. 4a**). The featureless matrix could believe to be the graphite-like amorphous carbon (more discussion under TEM analysis, **Fig. 5**). It is worthy to note that Raman spectral (**Fig. 2**) and XPS (**Fig. 3**) analyses already evidenced the presence of carbon in ZSV, ZV and SV samples. Further, FESEM-EDS study (**Fig. 4b1**) on compositional (atomic percentage, at%)

View Article Online
DOI: 10.1039/C5RA12322D

analysis for Zn and Cl of the hierarchical microstructures as given in **Figure 4b** which shows about 67.3% Zn and 32.7% Cl (Zn to Cl atomic ratio, R_{ZC} = 2.06). The source of Zn and Cl could be the simonkolleite nanopetals as evident from XRD patterns (**Fig. 1**) of the ZSV sample. It is interesting to note that the ZSA sample (obtained from ZSG gel after curing at 450^{o}C under air atmosphere) shows spherical clusters (size, 20±5 nm) (**Fig. 4c** and its **inset**). These clusters could be the mixtures of tetragonal-SnO_2 and orthorhombic zinc oxychloride as confirmed from the XRD patterns (**Fig. 1**) of the sample. On the other hand, the FESEM microstructure (d) of ZV displays the presence of nano petal/plate–like particles (thickness, 23-30 nm) that could be for rhomhedral simonkolleite/hexagonal ZnO as evident from the XRD patterns (**inset, Fig. 1**) of the sample. The R_{ZC} value calculated from the FESEM-EDS curve (**Fig. 4d1**) of the microstructure (**Fig. 4d**) could be comparable with the R_{ZC} value of ZSV. This result implied that the ZV sample also contains simonkolleite as identified from its XRD curve (**Fig. 1**). It is worthy to note that flower-like morphology constructed by hexagonal plates (**Fig. S5a, ESI**) was found in ZS$^{/}$V sample by curing initially at 450^{o}C under vacuum and finally, at 300^{o}C in pure oxygen of ZS$^{/}$G gel that was prepared from the precursor sol without using acetylacetone. Thereofore, it could appear that the formation of petal-like morphology of simonkolleite is possible in the sample derived from the precursor sol with acetylacetone. Although, the exact role of acetylacetone towards the formation of simonkolleite was not known but the graphite-like amorphous carbon in-situ generated in the nanocomposite, would help to form the morphology.[44] It should mention that the SV sample consisting of t-SnO_2 (**Fig. 1**) shows only spherical nano clusters (size, 17±2 nm) as revealed from FESEM study (**Fig. S5b, ESI**).

Simonkolleite is an important mineral with complex structure of the transition metal (Zn) layered hydroxide chloride.[27] It usually exists as hexagonal sheets.[17] Sometimes, depending upon the synthesis parameters, the formation of hierarchial structures could be

View Article Online
DOI: 10.1039/C5RA12322D

possible.[26,27] However, no distinct mechanism on the formation of hierarchial structures was available in the literature. Mahmoudian et. al[27] electrodeposited simonkolleite flower-like nanostructure on porous surface of zinc, coated with poly-(N-methyl pyrrole). The authors considered the trapping of Cl^- and OH^- ions within the pores of coatings, could be the reason for the morphology. In the present work, the formation of petal-like hierarchial structure of simonkolleite could be due to the curing of the precursor gels under vacuum. This is because various chemisorption and desorption processes as well as oxygen diffusion mechanisms are greatly involved during the curing process.[8]

3.4.2 TEM study

Figure 5 displays the field emission transmission electron microscope (FE-TEM) characterization result of ZSV nanocomposite. The TEM image of the sample shows flower-like hierarchical microstructure (**Fig. 5a**) decorated well with SnO_2 nanoparticles (average size, ~16 nm; histogram, **inset** of **Fig. 5b**). The HRTEM image (**inset A, Fig. 5b**) of the nanoparticle (A) shows distinct lattice fringes with interplanar distance, *d* (0.33 nm) matched with the tetragonal-SnO_2 nanocrystals [JCPDS Card 41-1445]. This observation fully supported the XRD result (**Fig. 1**) of the sample. The SAED pattern (**Fig. 5c**) for the microstructure as displayed in **Figure 5a** shows several bright spots and the calculated *d* values from the spots corresponded to orthorhombic simonkolleite and tetragonal SnO_2 nanoctystals. On the other hand, TEM-EDS (**Fig. 5d**) compositional (atomic percentage, at%) analysis for Zn, Sn and Cl elements for the hierarchical microstructure as displayed in **Figure 5a** shows the presence of about 56.7% Zn, 27.2% Cl and 16.1 % Sn with Zn to Cl (R_{ZC}), 2.08. It is worthy to mention that similar R_{ZC} value on the petal-like microstructure was obtained by the FESEM-EDS analysis (**Fig. 4b1**). Moreover, a typical TEM image (**Fig. 5e**) at higher magnification of ZSV sample shows the nanoparticles are embedded intimately in a

View Article Online
DOI: 10.1039/C5RA12322D

matrix. The HRTEM (**Fig. 5f**) of square marked portion as displayed in **Figure 5e** confirms the presence of distinct lattice fringes with interplanar distance, *d* (0.33 nm) matched with tetragonal-SnO_2 nanocrystals [JCPDS Card 41-1445] embedded in the mesoporous milky diffraction background. This background could suggest the presence of carbon[45] in the nanocomposite. It is also noted that in several portion of the matrix, the signature of graphitic layers[29] with relatively shorter interplanar distance (0.29 nm) than graphene[46] were observed. The shortening of interplanar distance would be considered as a consequence of the vacuum curing of precursor gels. Therefore, in the present work, the existing carbon matrix in the sample could be termed as graphite-like amorphous carbon which is found to be some what disorder structure.[29] It is to be mentioned that the presence of carbon in ZSV nanocomposite is already confirmed by Raman (**Fig. 2**) and X-ray photoelectron spectroscopy analyses (**Fig. 3**).

4.5 TG-DSC study

Thermal stability vis-à-vis thermal weight loss behaviour of ZSV sample having graphite-like amorphous carbon (**Figs. 2**, **3, 5**) was investigated by TG-DSC analysis (**Fig. 6**). The DSC curve shows two endothermic peaks appeared below 200^oC with the corresponding weight loss of about 4% as measured from the TG curve. This weight loss could be attributed to the loss of adsorbed water.[42,43] It is also seen from the DSC curve that the pyrolysis (exothermic) reaction, starts at ~350^oC and ends at ~530^oC. From the TG curve, up to ~ 530^oC, there is a total weight loss of 23.1% but above 530^oC, no further weight loss was measured from the sample. Hence, considering the loss of water, the further loss of about 19% could be ascribed to the loss of carbon along with the weight loss that happened for the conversion of simonkolleite [$Zn_5(OH)_8Cl_2.H_2O$] to ZnO as evidenced from the XRD (**Fig. S2**) study. It is worthy to mention that the presence of carbon in the sample was already confirmed from the

View Article Online
DOI: 10.1039/C5RA12322D

Raman, XPS and HRTEM analyses (**Figs. 2**, **3, 5**). Moreover, about 18% of canbon in the sample was measured by carbon determinator (**Table S3**). Therefore, in the sample, the amount of carbon obtained from the TG-DSC analysis (**Fig. 6**) is approximately matched with the data from carbon determinator.

3.6 Textural property

Textural property (surface area, pore size) of ZSV (**Fig. 7a**) and ZS$^{/}$V (**Fig. 7b)** nanocomposites were measured from BET nitrogen adsorption-desorption method. The isotherms of both the nanocomposites highlight IUPAC type IV architecture having H3 hysteresis loop, indicating the presence of slit-like mesopores in the samples.[47] The pore size distribution curves were drawn from the desorption branch of the isotherms (insets of **Figs. 7a,b**). From the distribution curves, the calculated average pore sizes were 3.1 nm and 3.5 nm for ZSV and ZS$^{/}$V, respectively. It is worthy to note that very high BET specific surface area of 142.6±0.2 m^2/g was obtained from the isotherms of ZSV sample. The presence of graphite-like carbon[29] as evidenced from Raman spectra (**Fig. 2**), TEM microstructural (**Fig. 5**) and XPS analysis (**Fig. 3**) of the sample could be the reason for the generation of the high surface area. This is true because in absence of the carbon (**Fig. 2**) in ZS$^{/}$V sample, the measured surface area was more than 4.5 times low (31.6±0.2 m^2/g) than ZSV. Due to this large surface area in ZSV, the surface active sites could increase and this typical textural property of the nanocomposite could be beneficial for obtaining its high photocatalytic activity towards degradation of organic dye under light illumination (discussed later).

3.7 Photocatalytic activity

Photodecomposition (**Fig. 8a,b, Table S4** of **ESI**) of Rhodamine 6G dye (10^{-5} M aqueous solution) using ZSV nanocomposite as photocatalyst was performed under UV illumination

View Article Online
DOI: 10.1039/C5RA12322D

(wavelength, 254 nm) after keeping the dye solution in presence of the sample at an optimum time of 30 min to attain dye adsorption equilibrium under dark condition (see **Fig. S6, ESI** for details). It was seen that the dye in the water solution decomposed completely in 32 min of the UV exposure. We also determined the dye decomposition rate constant, *k* by plotting *ln* (C_o/C) versus time, considering first order reaction kinetics. Here, C_o is the initial concentration and *C* denotes the remnant dye concentration at different times of UV exposure. All the plots are found to fit approximately linear; implying pseudo first-order reaction kinetics of the dye degradation. Using ZSV sample having graphite-like amorphous carbon, we obtained the *k* value, 0.096 min^{-1} (**inset, Fig. 8b**). It is worthy to note that the carbon-free nanocomposite, ZS/V owning simonkolleite and SnO_2 nanoheteroctures in presence of non-semiconductor zinc oxychloride (**Fig. 1**) as evident from XRD (Fig. 1) and Raman spectral results (**Fig. 2**) which showed nearly seven times lower *k* value (0.0145 min^{-1}) (**inset, Fig. 8c**) compare to the *k* value of ZSV. Also, other samples (ZSA, ZV and SV) showed very low rate constant (0.001 – 0.0045 min^{-1}) (**insets, Fig. 8d and Fig. S7a,b; Table S4, ESI**). Therefore, in this synthesis process, the single metal oxide nano semiconductor coupled with graphite-like amorphous carbon in ZV and SV samples or the carbon-free simonkolleite/SnO_2 nanoheteroctures showed very negligible photocatalytic activity; although the crystallite (**Table S6**) / particle sizes (**Figs. 4, 5; Fig. S4, ESI**) of simonkolleite and SnO_2 in all the samples were in the nano domain which could have possibility of forming photogenerated charges (electrons and holes) with stronger oxidative/reductive capabilities. In this work, the presence of carbon in the mesoporous (average pore size, 3.1 nm) ZSV nanocomposite with large specific surface area (142.6±0.2 m^2/g, measured by BET nitrogen adsorption-desorption isotherms, **Fig. 7a**) could help to create more and more contacts with the dye molecules on the catalyst surface.[36] Moreover, the carbon could possibly improve the separation efficiency of photogenerated charge carriers via interfacial interactions with the

View Article Online
DOI: 10.1039/C5RA12322D

nanoheterostructures (see **Fig. 9** for more details). This could consequence an improvement of photocatalytic activity of the ZSV nanocomposite towards degradation of organic pollutant like Rhodamine 6G under UV illumination. Moreover, the reusability test (**Fig. S3, Table S5**) of ZSV photocatalyst shows only 5 percent decrease in the dye decomposition efficiency after five successive recycles for 32 min UV exposure in each cycle. The slight decrease of the photocatalytic activity of ZSV could be attributed to an oxidation of the carbon by energetic valence band holes (h^+) generated in the photochemical reaction. However, the oxidation process was seemed to be very slow and the high concentration of the dye could greatly compete with the hole scavenging process.[48] It is also true that the photocatalytic activity could reduce due to photo corrosion of nano semiconductors (simonkolleite and SnO_2). However, the presence of graphite-like amorphous carbon would inhibit the photo corrosion effectively.[48] In this respect, the ZSV sample as a new sol-gel nanocomposite showed better with few exceptions (**Table S7, ESI**) than other photocatalysts reported in the literatures.[49-53] Therefore, the ZSV nanocomposite could be considered as a new, cost effective and highly efficient photocatalyst towards degradation of organic pollutant like Rhodamine 6G dye under the UV illumination.

It is known[48,54-60] that charge carrier (electron and hole) separation and electron transport behaviours of semiconductors are the critical factors in photocatalytic dye decomposition reactions. The behaviours could clearly be understood from the study of powerful electrochemical impedance spectroscopy (EIS). In this respect, the smaller arc radius in the EIS semicircle of an electrode (photocatalyst) under suitable light irradiation could indicate an effective separation of photo-generated electron–hole pairs as well as the fast interfacial charge transfer. Moreover, the presence of one arc/semicircle on the EIS plane implies an involvement of only surface charge-transfer step in the photocatalytic reaction and the magnitude of arc radius could have relation with the rate of degradation reaction.

View Article Online
DOI: 10.1039/C5RA12322D

Therefore, several authors[48,54-60] efficiently utilized the EIS tool to explain the photocatalytic activity of semiconductors including carbon coupled single / mixed metal oxide nanocomposites (see text with **Table S8 of ESI** for more details). In the present work, the EIS was performed on ZSV nanocomposite as well as on other samples (ZS$^{/}$V, ZSA, ZV and SV) to understand the difference in charge separation behaviour which could directly relate to the photocatalytic activities towards degradation of rhodamine 6G dye as observed under UV illumination (**Table S4 and Fig. S7**, **ESI**). The EIS Nyquist plots of UV illuminated (λ, 254 nm) photo-electrodes are displayed in **Figure 9.** The plot of samples shows only one arc/semicircle on the EIS plane display, indicating only the surface charge-transfer could occur in the electrodes.[20,48] Moreover, the radius (r) of arc/semicircle in the Nyquist plots for the ZSV, ZS$^{/}$V, ZSA, ZV and SV photo-electrodes decreases in the order, $r_{sv} > r_{zv} > r_{zsA} > r_{zs^{/}v} > r_{zsv}$. A similar trend was also observed in the change of magnitude of arc/semicircle for the samples under dark condition (not shown here). This result obviously implies that the capability of most effective photogenerated charge separation / reduction of the recombination rate of the charges was happened in ZSV.[48] It could also indicate that the fastest interfacial charge transfer to acceptor/donor could happened in the ZSV sample where the graphite-like amorphous carbon is present as evident from the Raman spectral (**Fig. 2**), XPS (**Fig. 3**), carbon content (**Table S3, ESI**) and TEM (**Fig. 5**) analyses of the sample. This phenomenon could be possible via an interfacial interaction between the carbon and the nanoheterostructures made by simonkolleite nano petals and SnO_2 nano particles. This assumption could be justified from the experimental observation of much higher arc radius (in the EIS plot) compare to ZSV as obtained from carbon-free ZS$^{/}$V sample (confirmed by Raman spectral study, **Fig. 2**). It is worthy to note that both the samples possessed simonkolleite nano petals/nano SnO_2 nanoheterostructures. It is also important to mention that the change in magnitude of arc/semicircle in the Nyquist plots of the samples was

View Article Online
DOI: 10.1039/C5RA12322D

consistent with the photocatalytic activities in terms of the dye degradation rate constant (k) under UV illumination. This improved electrochemical property of ZSV nanocomposite towards the photocatalytic activity would rely on the electron transport properties of graphite-like amorphous carbon.[20] It has already been reported by many authors that relatively higher photocatalytic efficiency (PE) could be obtained in nanoheterostructures semiconductors (like simonkolleite/TiO_2, ZnO/SnO_2, ZnO/TiO_2 etc).[18,61,62] Therefore, in the present work, it implies the carbon that strongly coupled with the simonkolleite petals and SnO_2 nanoheterostructures in ZSV sample, could further improve the PE and made the nanocomposite as a highly efficient photocatalyst towards degradation the dye. In this respect, the higher specific surface area of ZSV sample as measured by BET nitrogen adsorption-desorption isotherms (**Fig. 7**) due to presence of the carbon, was also a beneficial factor for the improvement of the photocatalytic activity.[11] In the same vein, due to its large surface area the surface active sites in the photocatalyst could increase and consequently, more and more dye molecules could come into contact with the surface of the catalyst.[48,63] As a result, an effective photocatalytic reaction could be happened for the ZSV sample. In this respect, many authors had already reported the effect of surface area on the photocatalytic activity (rate constant) of different photocatalysts including carbon based composite semiconductor materials on different organics (see details in **Table S9,10 of ESI**).

It is worthy to note[11-13] that the carbon (e.g. graphene, carbon nano tube, amorphous carbon) could couple with several basic materials (such as oxides, metals, polymers) even with heterostructures to advance the functional properties including optoelectronic property of the materials. In this regard, major studies had already been done on carbon (C) coupled single metal oxide semiconductor (such as ZnO/C, SnO_2/C, TiO_2/C) composites for enhancing the photocatalytic activity of semiconductors.[11-13] Also, carbon coupling mixed metal oxide semiconductors (e.g. α-Fe_2O_3/Mn_3O_4/graphene), which showed excellent charge

View Article Online
DOI: 10.1039/C5RA12322D

transfer performance for photocatalytic water oxidation.[14] It is also known that in the carbon-coupled nanocomposite, the photogenerated electrons would accumulate on the carbon surface to convert O_2 to $O_2^{\bullet}$ and the holes could remain on the semiconductor surface transforming H_2O or ^{-}OH to $^{-}OH^{\bullet}$, useful for fast degradation of organic dye by the generated free radicals.[15,64] On the other hand, the carbon could enhance the textural property (particularly surface area and porosity) that could necessary for effective contact of photodegradable organic dyes on the surface of photocatalysts. Therefore, in the present work, the dual role of the carbon was found; one role for faster rate of interfacial charge transfer and another for enhancing specific surface area of the ZSV nanocomposite. On the other hand, simonkolleite is now recognized as one of the wide band gap semiconductors having electronic band structure similar to ZnO (bulk band gap energy, 3.3 eV).[17] Moreover, it could able to decompose organic dye. It is also known that the electrochemical/photochemical property of SC could improve by coupling with TiO_2[18] as heterostructures. SnO_2 is a well-known metal oxide semiconductor having widespread applications.[11] However, the photocatalytic activity of SnO_2 is low.[19] In this work, it could be expected that the photogenerated electrons of SC would transfer to SnO_2 as the electronic band structure of SC is similar to ZnO.[17] This would result a wide separation vis-à-vis reduction in recombination rate of charge carriers. Moreover, the carbon in the nanocomposite could further enhance the photogenerated charge separation in the photo-responsive materials through accelerating electron transport in addition to improve the textural property (such as surface area, porosity) that could be the favourable factor for enhancing active sites of the photocatalyst under UV illumination.[20] In this respect, we should mention that α-Fe_2O_3/Mn_3O_4/graphene composite, reported very recently as a highly efficient photocatalyst for water oxidation.[14]

View Article Online
DOI: 10.1039/C5RA12322D

It is known that an optimum content of carbon could require for obtaining efficient photocatalytic activity in carbon coupled photocatalyst towards decomposition of water pollutants (such as organic dyes).[65,66] Therefore, it is absolutely necessary to verify whether ~18% graphite-like amorphous carbon that present in ZSV could be an optimum content of carbon for the purpose. In this respect, we changed the carbon content in the nanocomposites by varying acetylacetone content in the two more precursor sols and obtained ~7% and 23.5% carbon (**Table S3, ESI**) as analyzed by carbon determinator in ZSV-LC and ZSV-HC, respectively. It was seen that ZSV-LC showed comparatively low value of first order rate constant ($k = 0.043\ min^{-1}$; ~ 100% dye decomposition in 64 min) than ZSV for the dye decomposition (**Fig. S8, ESI**) under the UV exposure. However, an interesting result was obtained from ZSV-HC sample. It is noted that by keeping the ZSV-HC sample with continuous stirring in the dye solution for 64 min under the dark condition, a complete adsorption of the dye was seen (**Fig. S8, ESI**). This strong adsorption capability but low photocatalytic dye decomposition activity (~57% dye decomposed in 60 min under the UV) of ZSV-HC compare to ZSV-LC and ZSV samples discussed elaborately in the ESI (**Fig. S8**). Hence, it is clear that the ZSV-HC sample was an efficient dye adsorbent not as an efficient photocatalyst. This adsorption capability of the ZSV-HC could be ascribed to the presence of excess content of the carbon. Possibly, the excess carbon could create shielding effect of incident UV light[65,66] and covered the active sites of nanoheterostructures (simonkolleite nanopetals/quasi-spherical tin oxide nanoparticles) in the nanocomposite. In case of ZSV-LC, the lowest carbon content would not be sufficient for the separation vis-à-vis reduction in recombination rate of photogenerated charge carriers (electron and hole).[59,67] Therefore, an optimum carbon content of ~18% (**Table S3**) in ZSV sample could be required for maximizing the photocatalytic activity towards decomposition of rhodamine 6G dye under UV exposure.

View Article Online
DOI: 10.1039/C5RA12322D

It is known that several reactive species (RES) could produce during the photocatalytic dye decomposition reactions.[64] Their generation could be understood by the use of specific RES scavenger (such as *tert*-butyl alcohol, TBA; potassium iodide, KI; 1,4-benzoquinone, BQ). Therefore, many authors used TBA, KI and BQ in the dye solution to examine the formation of $^{\bullet}OH$ (hydroxyl radical), h^+ (hole) and $^{\bullet}O^{2-}$ (superoxide radical), respectively. In our present work, we also used these scavengers for the purpose of understanding the existence of specific RES that took part in the dye decomposition reaction. As can be seen from **Figure S9** (**ESI**), 1 mM BQ solution could completely terminate the dye degradation reaction by consuming/arresting $^{\bullet}O^{2-}$ radicals that play a significant role in the photocatalytic reaction. Moreover, on addition of 10 mM TBA / 2 mM KI solution, the dye degradation was also found to decrease significantly. Therefore, the RES scavenger experiment clearly indicated that the $^{\bullet}O^{2-}$ and $^{\bullet}OH$ radicals as well as h^+ ions could generate for the degradation of Rh6G dye under UV illumination. The photochemical reactions could be proposed (equations 1 to 8) depending on the free radical scavenger experiment.[10]

$$SnO_2\text{-SC/Carbon} + h\nu \longrightarrow SnO_2(e_{CB}^-) + SC(h_{VB}^+) + Carbon \quad \text{- - - (1)}$$

$$SnO_2(e_{CB}^-) + Carbon \longrightarrow SnO_2 + Carbon(e_{CB}^-) \quad \text{- - - (2)}$$

$$Carbon(e_{CB}^-) + O_2 \longrightarrow Carbon + {}^{\bullet}O_2^- \quad \text{- - - (3)}$$

$$SC(h_{vb}^+) + OH^- \longrightarrow SC + {}^{\bullet}OH \quad \text{- - - (4)}$$

$${}^{\bullet}O_2^- + H_2O \longrightarrow HO_2^{\bullet} + OH^- \quad \text{- - - (5)}$$

$$HO_2^{\bullet} + H_2O \longrightarrow OH^{\bullet} + H_2O_2 \quad \text{- - - (6)}$$

$$H_2O_2 \longrightarrow 2OH^{\bullet} \quad \text{- - - (7)}$$

$$Rh\ 6G + OH^{\bullet} \longrightarrow \text{Degradation product} \quad \text{- - - (8)}$$

View Article Online
DOI: 10.1039/C5RA12322D

4. Conclusion

This report discloses a new sol-gel nanocomposite having rhombohedral simonkolleite nano petals and quasi-spherical tetragonal SnO_2 nanoparticles forming nanoheterostructures embedded in graphite-like amorphous carbon as efficient and reusable photocatalyst, synthesized under vacuum curing (450^oC) of precursor gel derived from the sol (Zn : Sn = 2 : 1) in 2-methoxy ethanol with acetylacetone. The sample showed high photocatalytic activity (10^{-5}M dye solution degraded completely in 32 min) under UV illumination. Reusability test of the photocatalyst exhibited about 95% of dye degradation after five successive recycles. In the nanocomposite, an active role of the carbon in an optimum content (~18%) was found to generate high BET specific surface area (~143 m^2/g) and also to accelerate photo-induced charge carrier separation and electron transport in the nanoheterostructures. This simple synthesis strategy could open a new avenue to develop sol-gel nanocomposites as efficient and reusable photocatalysts from simonkolleite based other nanoheterostructures, embedded in graphite-like amorphous carbon.

5. Acknowledgements

Authors wish to acknowledge the Director, CSIR-Central Glass and Ceramic Research Institute, Kolkata for his kind permission to publish this work. MP and SB thank UGC and CSIR, Govt. of India for providing their research fellowships. The authors also acknowledge the help rendered by Analytical Facility, Glass, Bioceramic and Coating as well as Nanostructured Materials Divisions for several characterizations of samples. The work has been done as an associated research work under CSIR funded Supra Institutional Network Project (SINP) (No. ESC0202) of 12th Five Year Plan.

View Article Online
DOI: 10.1039/C5RA12322D

References

1 M. R. Hoffmann, S.T. Martin, W. Choi and D. W. Bahnemann, *Chem. Rev*., 1995, **95**, 69–96.

2 Y. -M. Zheng, R. F. Yunus, K.G. N. Nanayakkara and J. P. Chen, *Ind. Eng. Chem. Res.*, 2012, **51**, 5953–5960.

3 X. Wu, X. Xu, C. Guo and H. Zeng, *J. Nanomater.*, 2014, **2014**, 603096 (2 pages).

4 R. S. Dhabbe, A. N. Kadam, M. B. Suwarnkar, M. R. Kokate and K. M. Garadkar, *J. Mater. Sci. Mater. Electron.*, 2014, **25**, 3179–3189.

5 M. Pal, S. Bera, S. Sarkar and S. Jana, *RSC Adv*., 2014, **4**, 11552–11563.

6 F.T. Vasco and A. V. Kuznetsov, "Electronic states and optical transitions in semiconductor heterostructures", Springer, New York, 1998.

7 S. Jana, A. S. Vuk, A. Mallick, B. Orel and P. K. Biswas, *Mater. Res. Bull.*, 2011, **46,** 2392–2397.

8 M. Pal, S. Bera and S. Jana, *J. Sol-Gel Sci. Technol*., 2013, **67**, 8–17.

9 M. Pal, S. Bera, S. Sarkar and S. Jana, *Int. J. Eng. Innov. Technol*., 2014, **3**, 158–163.

10 M. T. Uddin, Y. Nicolas, C. Olivier, T. Toupance, L. Servant, M. M. Muller, H.-J. Kleebe, J. Ziegler and W. Jaegermann, *Inorg. Chem.*, 2012, **51**, 7764–7773.

11 G. Malekshoar, K. Pal, Q. He, A. Yu and A. K. Ray, *Ind. Eng. Chem. Res.*, 2014, **53**, 18824–18832.

12 C. Peng, S. Zhang, D. Jewell and G. Z. Chen, *Prog. Nat. Sci.*, 2008, **18,** 777–788.

13 W. -Q. Han and A. Zettl, *Nano Lett.*, 2003, **3**, 681–683.

14 S. Yin, X. Wang, Z. Mou, Y. Wu, H. Huang, M. Zhu, Y. Du and P. Yang, P*hys. Chem. Chem. Phys.*, 2014, **16**, 11289–11296.

15 Y. Zhao, M.-Y. Ma, G.-W. Cui, X.-F. Shi, F.-Y. Han, X.-Y. Xia and B. Tang, *Carbon*, 2014, **73**, 333–337.

View Article Online
DOI: 10.1039/C5RA12322D

16 J. D. Yoo, P. Volovitch, A. A. Aal C. Allely and K. Ogle, Corros. Sci., 2013, **70**, 1–10.

17 H. Chen, L. Zhu, H. Liu and W. Li, *Electrochim. Acta*, 2013, **105**, 289–298.

18 M. I. Badawya, M. E.M. Ali, M. Y. Ghaly and M. A. El-Missiry, *Process Saf. Environ. Prot.*, 2015, **94**, 11–17.

19 Z. Zhang, C. Shao, X. Li, L. Zhang, H. Xue, C. Wang and Y. Liu, *J. Phys. Chem. C*, 2010, **114**, 7920–7925.

20 J. Du, X. Lai, N. Yang, J. Zhai, D. Kisailus, F. Su, D. Wang and L. Jiang, *ACS Nano*, 2011, **5**, 590–596.

21 C. Klinke and K. Kern, *Nanotechnol.*, 2007, **18**, 215601 (4 pages).

22 R. A. Aziz and I. Sopyan, *Indian J. Chem.*, 2009, **48**, 951–957.

23 P. Innocenzi and T. Kidchob, *J. Sol-Gel Sci. Technol*., 2005, **35**, 225–235.

24 C. Mateous–Pedreroa, H. Silvaa, D. A. P. Tanaka, S. Liguori, A. Iulianelli, A. Basile, A. Mendes, *Appl. Catal. B: Environ*., 2015, **174**, 67–76.

25 S. Cousy, L. Svobod, J. Zelenka, *Nanocon*, 2013, **10**, 16–18.

26 W. Zhang and K. Yanagisawa, *Chem. Mater.*, 2007, **19**, 2329–2334.

27 M. R. Mahmoudian, W. J. Basirun, Y. Alias and M. Ebadi, *Appl. Surf. Sci*., 2011, **257,** 10539–10544.

28 R. D. Roy, D. Sil, S. Jana, P. K. Biswas and S. K. Bhadra, Photonic Sens., 2012, **2**, 81–91.

29 V. Kulikovsky, K. Metlov, A. Kurdyumov, P. Bohac and L. Jastrabik, *Diamond Related Mater*., 2002, **11,** 1467–1471.

30 R. Saliger, U. Fischer, C. Herta and J. Fricke, *J. Non-Cryst. Solids*, 1998, **225**, 81–85.

31 D. Yang, A. Velamakanni, G. Bozoklu, S. Park, M. Stoller, R. D. Piner, S. Stankovich, I. Jung, D. A. Field, C. A. Ventrice Jr. and R. S. Ruoff, *Carbon*, 2009, **47**, 145–152.

32 A. C. Ferrari and J. Robertson, *Phil. Trans. R. Soc. Lond. A*, 2004, **362**, 2477–2512.

33 L. Zhang, H. Cheng, R. Zong and Y. Zhu, *J. Phys. Chem. C*, 2009, **113**, 2368–2374.

View Article Online
DOI: 10.1039/C5RA12322D

34 S. Zeb, M. Sadiq, A. Qayyum, G. Murtaza and M. Zakaullah, *Mater. Chem. Phys.*, 2007, **103**, 235–240.

35 P. K. Chu and L. Li, *Mater. Chem. Phys.*, 2006, **96**, 253–277.

36 T. Xia, W. Zhang, Z. Wang, Y. Zhang, X. Song, J. Murowchick, V. Battaglia, G. Liu and X. Chen, *Nano Energy*, 2014, **6**, 109–118.

37 M. Chen, X. Wang , Y.H. Yu, Z.L. Pei, X.D. Bai, C. Sun, R.F. Huang and L.S. Wen, *Appl. Surf. Sci.*, 2000, **158**, 134–140.

38 X. Shi, X. Zhao, L. Duan, H. Sun, J. Liu, X. Bai, M. Guan, M. Cao and J. Liu, *J. Sol-Gel Sci. Technol*., 2013, **66**, 301–305.

39 Z. Xiufeng, L. Juan, L. Lianghai and W. Zuoshan, *J. Nanomater.*, 2011, **2011**, 432947 (5 pages).

40 W.-S. Choi, *Trans. Electr. Electron. Mater.*, 2009, **10**, 200–202.

41 Y. Cao, T. He, L. Zhao, E. Wang, W. Yang and Y. Cao, *J. Phys. Chem. C*, 2009, **113**, 18121–18124.

42 C. G. Vassileva and S. V. Vassilev, *Fuel Process Technol.*, 2006, **87**, 1095–1116.

43 R. D. Roy, D. Sil, S. Jana, N. Bhandaru, S. K. Bhadra, P. K. Biswas and R. Mukherjee, *Ind. Eng. Chem. Res.*, 2012, **51**, 9546–9553.

44 M. Ramin and F. Taleshi, *Int. Nano Lett.*, 2013, **3**, 32 (6 pages).

45 T. Zhou , Y. Zheng , H. Gao , S. Min , S. Li , H. K. Liu and Z. Guo, *Adv. Sci.*, 2015, 1500027 (8 pages).

46 G. Wang, X. Shen, J. Yao and J. Park, *Carbon*, 2009, **47**, 2049–2053.

47 B. Rushton and R. Mokaya, *J. Mater. Chem.*, 2008, **18**, 235–241.

48 H. Fu, T. Xu, S. Zhu and Y. Zhu, *Environ. Sci. Technol.*, 2008***, 42***, 8064–8069.

49 S. Feraru, A.I. Borhan, P. Samoila, C. Mita, S. Cucu-Man, A.R. Iordan and M.N. Palamaru, *J. Photochem. Photobio. A Chem.*, 2015, **307-308**, 1–8.

View Article Online
DOI: 10.1039/C5RA12322D

50 W. Dong, Y. Sun, Q. Ma, L. Zhua, W. Hua, X. Lu, G. Zhuang, S. Zhang, Z. Guo and D. Zhao, *J. Hazard. Mater.*, 2012, **229-230**, 307–320.

51 A. Mills, A. Belghazi, R. H. Davies, D. Worsley and S. Morris *J. Photochem. Photobio. A Chem.*, 1994, **79**, 131–139.

52 C. Zhang, J. Zhang, Y. Su, M. Xu, Z. Yang and Y. Zhang, *Physica E*, 2014, **56**, 251–255.

53 K. K. Haldar, G. Sinha, J. Lahtinen, and A. Patra, *ACS Appl. Mater. Interfaces*, 2012, **4**, 6266–6272.

54 T. Xu, L. Zhang, H. Cheng and Y. Zhu, *Appl. Catal. B Environ.*, 2011, **101**, 382–387.

55 Y. Wang, F. Wang and J. He, *Nanoscale*, 2013, **5**, 11291–11297.

56 H. Yu, X. Quan, S. Chen, H. Zhao and Y. Zhang, *J. Photochem Photobio A Chem.*, 2008, **200**, 301–306.

57 M. Sun, X. Ma, Xi Chen, Y. Sun, X. Cui and Y. Lin, *RSC Adv.*, 2014, **4**, 1120–1127.

58 Y. Wang, Y. Zhang, G. Zhao, H Tian, H. Shi, and T. Zhou, *ACS Appl. Mater. Interfaces*, 2012, **4**, 3965–3972.

59 P. Xiong, Y. Fu, L. Wang and X. Wang, *Chem. Eng. J.*, 2012, **195-196**, 149–157.

60 S. A. Ansari, M. M. Khan, M. O. Ansari, J. Lee and M. H. Cho, *RSC Adv.*, 2014, **4**, 26013–26021.

61 W. Cun, Z. Jincai, W. Xinming, M. Bixian, S. Guoying, P. Ping'an and F. Jiamo, *Appl. Catal. B: Environ.*, 2002, **39**, 269–279.

62 S. Guo, S. Han, H. Mao, S. Dong, C. Wu, L. Jia, B. Chi, J. Pu and J. Li, *J. Power Sources*, 2014, **245**, 979–985.

63 M. Zeda, O. Wonchun, *Chinese J. Catal.*, 2012, **33**, 1495–1501.

64 C. Hu, Y. Lan, J. Qu, X. Hu and A. Wang, *J. Phys. Chem. B*, 2006, **110**, 4066–4072.

65 J. Zhang, J. Yu, M. Jaroniec and J. R. Gong, *Nano Lett.*, 2012, **12**, 4584−4589.

View Article Online
DOI: 10.1039/C5RA12322D

66 S. Zhuang, X. Xu, B. Feng, J. Hu, Y. Pang, G. Zhou, L. Tong and Y. Zhou, *ACS Appl. Mater. Interfaces*, 2014, **6**, 613−621.

67 N. T. Khoa, S. W. Kim, D. -H. Yoo, S. Cho, E. J. Kim, S. H. Hahn, *ACS Appl. Mater. Interfaces*, 2015, **7**, 3524–3531.

View Article Online
DOI: 10.1039/C5RA12322D

Figure captions

Fig. 1: XRD patterns of ZSV, ZS$^{/}$V, ZSA, ZV (inset) and SV samples.

Fig. 2: Raman spectra of ZSV nanocomposite along with ZS$^{/}$V, ZSA, ZV and SV samples. Inset indicates the Raman spectrum of ZS$^{/}$V sample cured at 450^{o}C under vacuum.

Fig. 3: XPS results of ZSV nanocomposite. (a) Survey spectrum shows the presence of different elements; (b) typical XPS data for the binding energy of C1s;(c) binding energy signal for O1s; (d) and (e) represent the binding energy signals for core levels of Zn2p and Sn3d, respectively.

Fig. 4: FESEM images of (a,b) ZSV, (c) ZSA and (d) ZV samples along with FESEM-EDS curves of (b1) and (d1) that are obtained from the microstructures (b) and (d), respectively. Zone (i) of (a) is magnified to (b) shows petal-like particles while zone (ii) of the enlarged part of image (a) displays quasi-spherical nanoparticles embedded in a freatureless matrix.

Fig. 5: TEM results of ZSV sample. (a) TEM image shows a petal shaped large particle decorated with nanoparticles embedded in freatureless matrix. A magnified marked portion of (a) is shown as (b) (inset shows the histogram for particle size distribution with average particle size, 10.5 nm). Inside the image (b), the HR-TEM of a particle (marked as A) is also given. The HR-TEM image shows distinct lattice fringes with d spacing matched with t-SnO_2 along (110) plane. The SAED of the microstructure (a) is displayed as (c), confirms the presence of both t-SnO_2 and o-simonkolleite nanocrystals. TEM-EDS of the microstructure (a) is shown in (d). The presence of different elements such as Zn, Sn, Cl, O, C etc are detected from the EDS curve with the contents of Zn (~66.2%), Cl (~26.4%) and Sn (~7.4%). The sample also shows a different microstructure as shown in (e). (f) is the magnified part (square marked) of (e), confirms the presence of both t-SnO_2 (from the lattice frignes) and graphite-like amorphous carbon matrix.

Fig. 6: TG-DSC curves of ZSV sample.

Fig. 7: BET nitrogen adsorption and desorption isotherms of ZSV and ZS$^{/}$V nanocomposites (insets show the pore size distribution curves constructed from desorption branch of the isotherms).

Fig. 8: Photocatalytic activity of ZSV, ZS$^{/}$V and ZSA samples towards degradation of rhodamine 6G dye under UV illumination. (a) Remnant dye concentration *versus* UV exposure time: (b), (c) and (d) visible spectra of dye solution at different illumination times for the photocatalysts; ZSV, ZS$^{/}$V and ZSA, respectively (insets show respective dye decomposition rate constant, considering first order reaction kinetics).

Fig. 9: Electrochemical impedence (EIS) Nyquist plots of electrodes of different samples obtained under UV (λ, 254 nm) illumination.

View Article Online
DOI: 10.1039/C5RA12322D

Figures

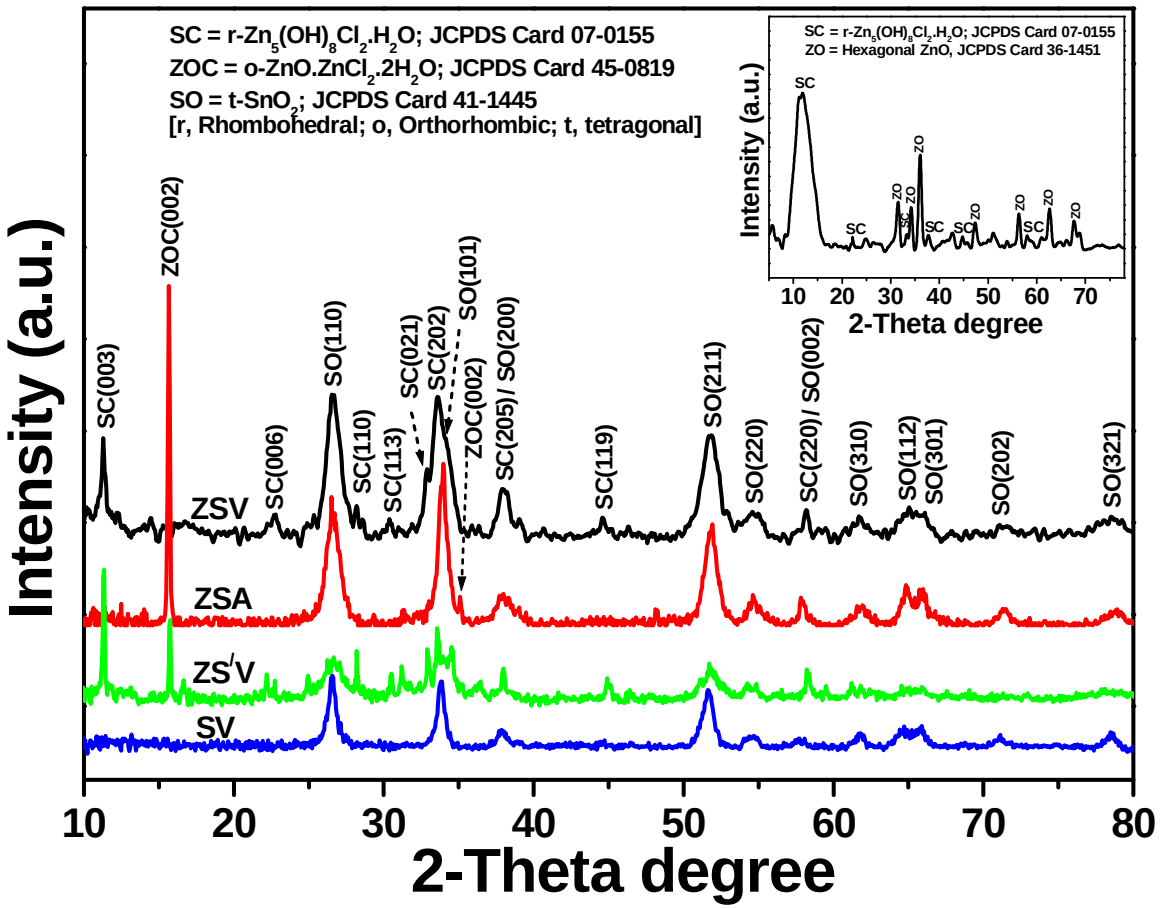

Fig. 1

View Article Online
DOI: 10.1039/C5RA12322D

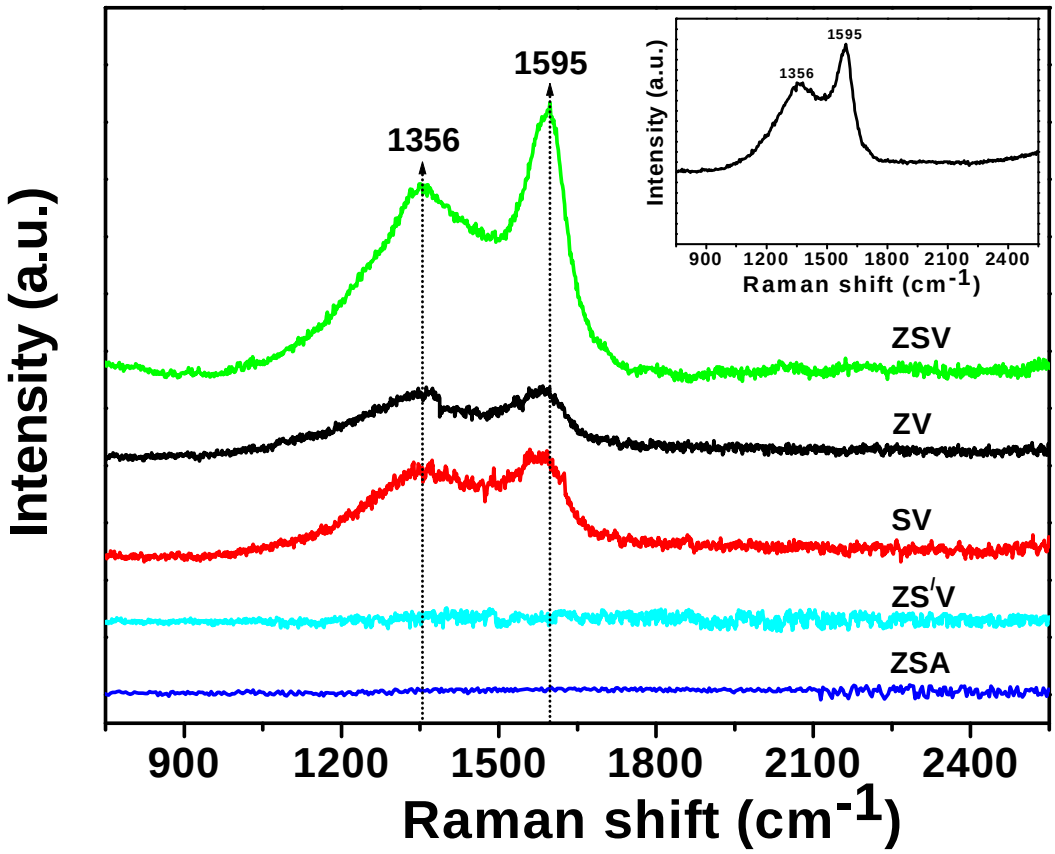

Fig. 2

View Article Online
DOI: 10.1039/C5RA12322D

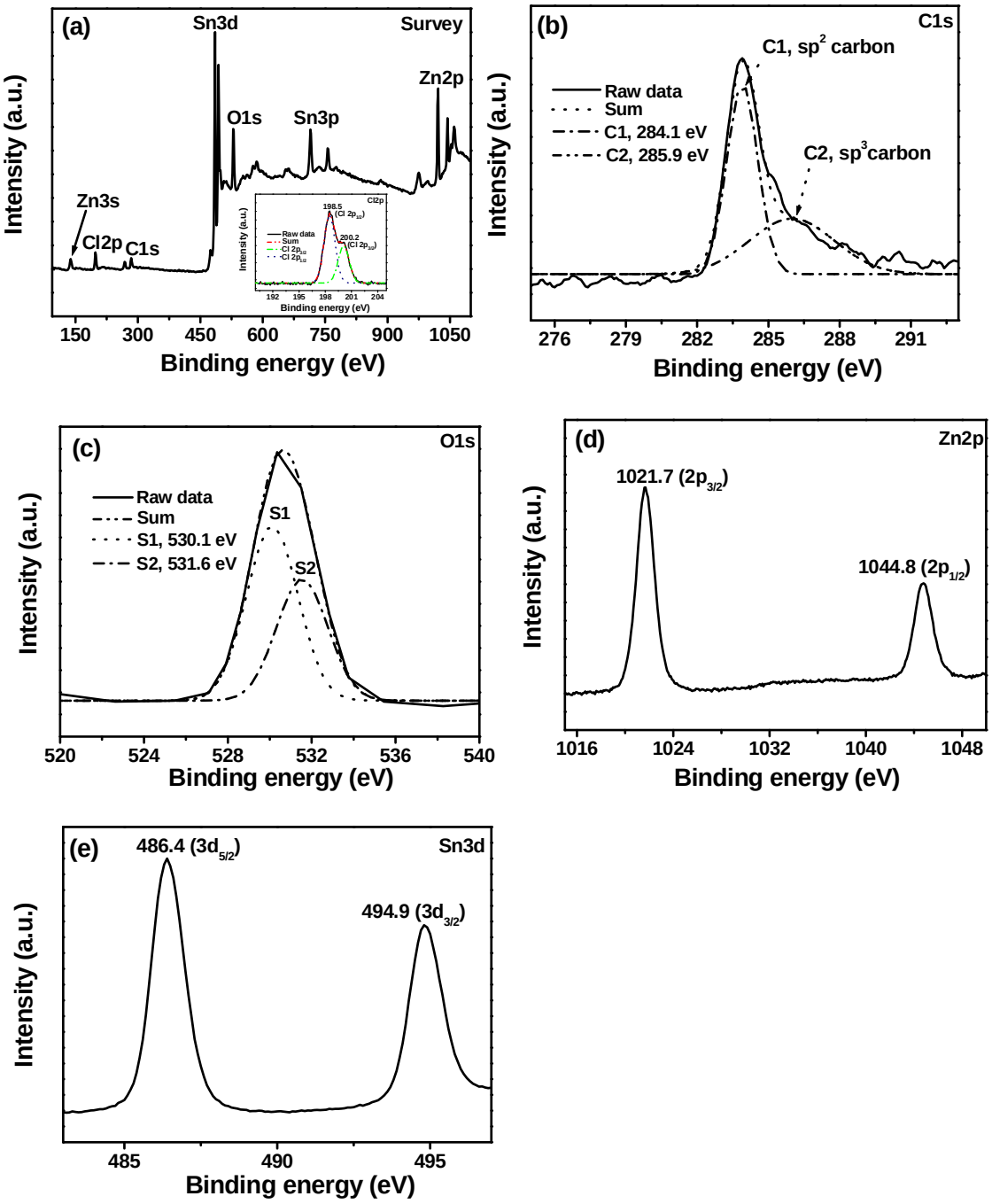

Fig. 3

View Article Online
DOI: 10.1039/C5RA12322D

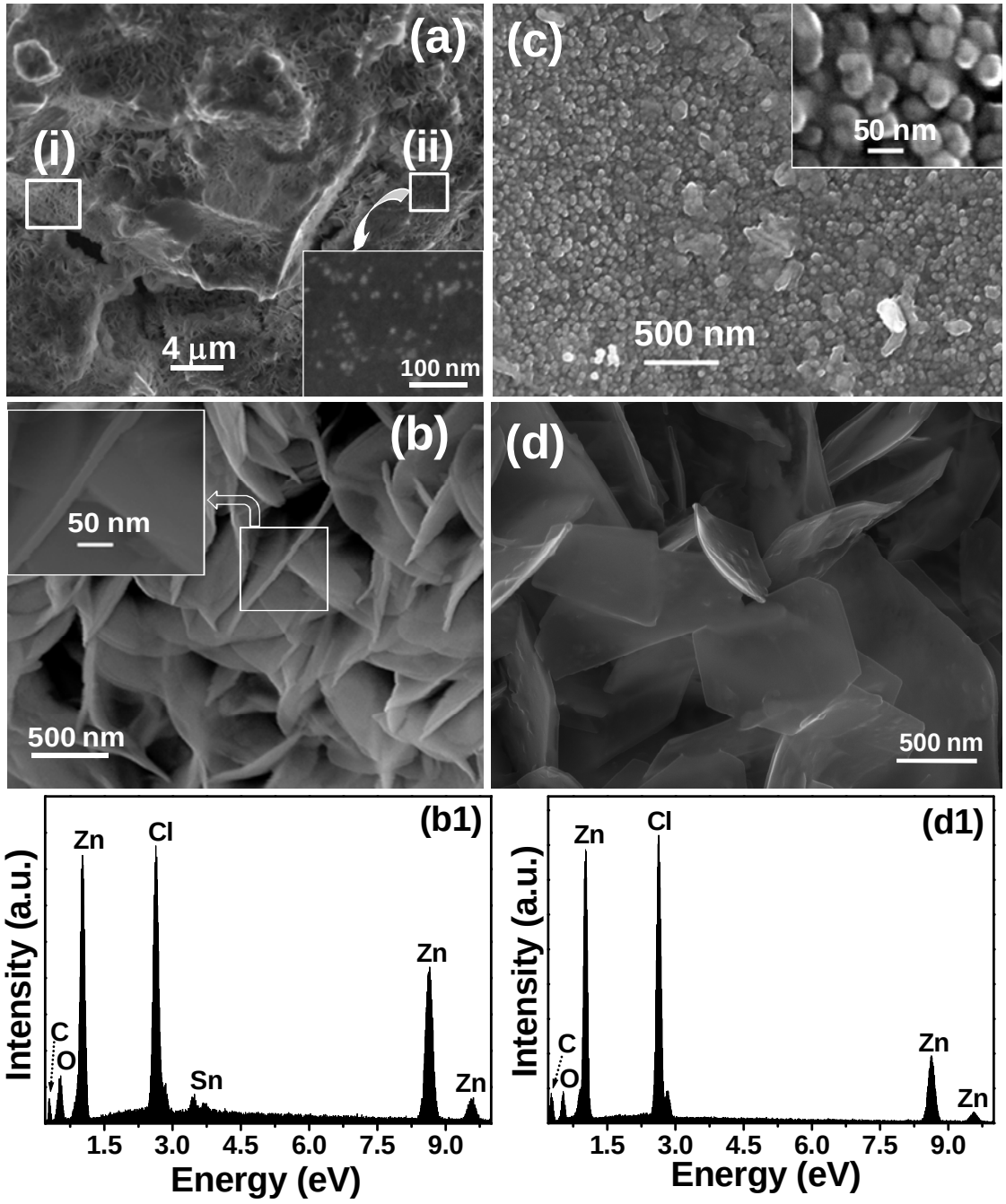

Fig. 4

View Article Online
DOI: 10.1039/C5RA12322D

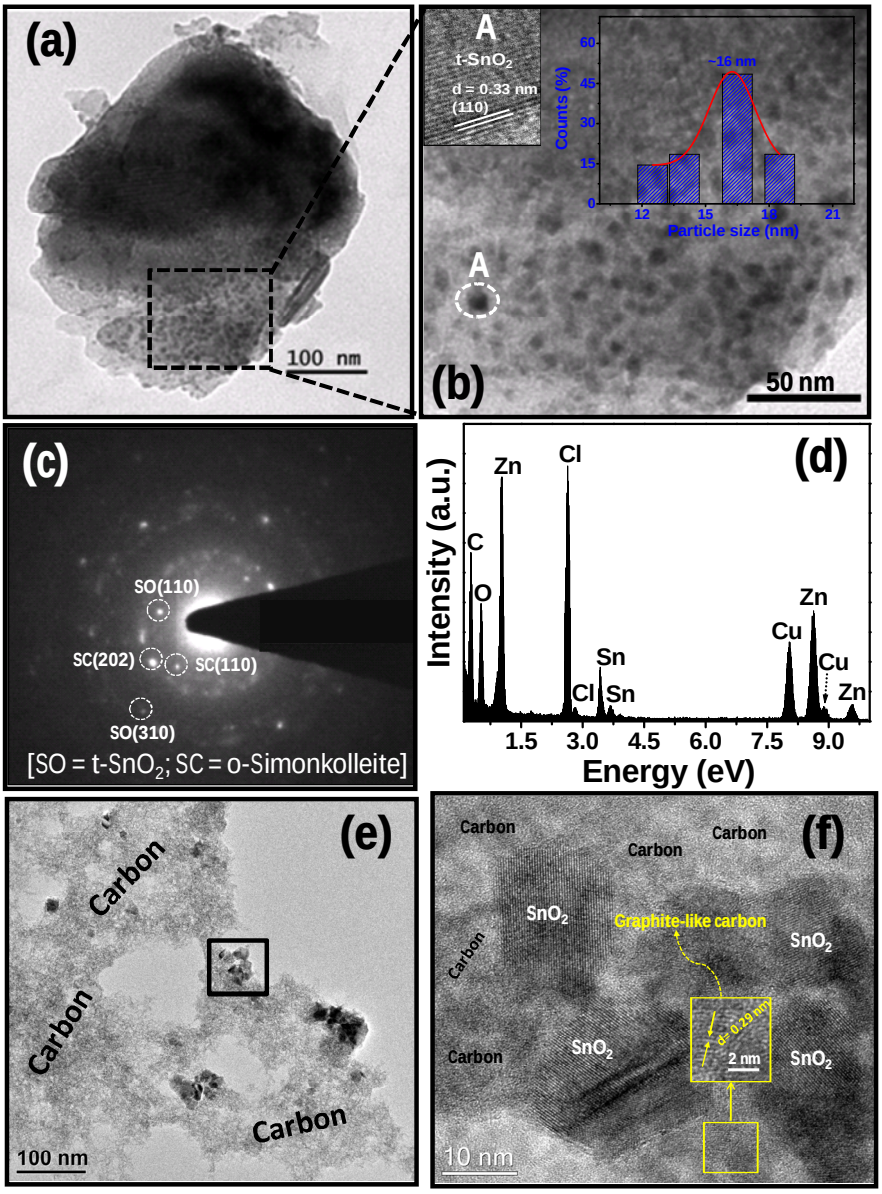

Fig. 5

View Article Online
DOI: 10.1039/C5RA12322D

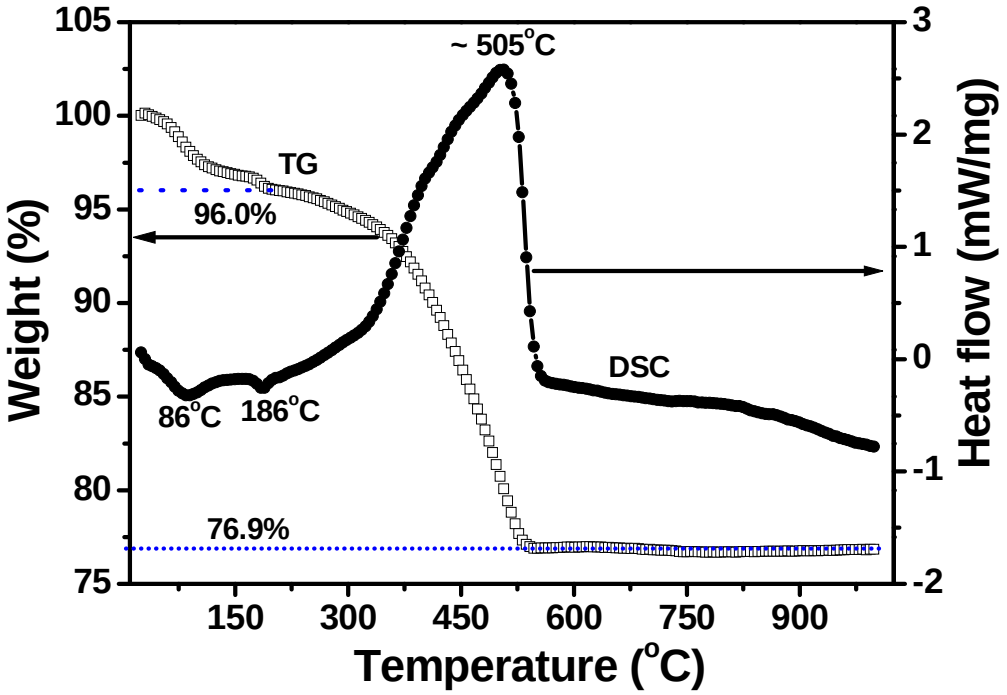

Fig. 6

View Article Online
DOI: 10.1039/C5RA12322D

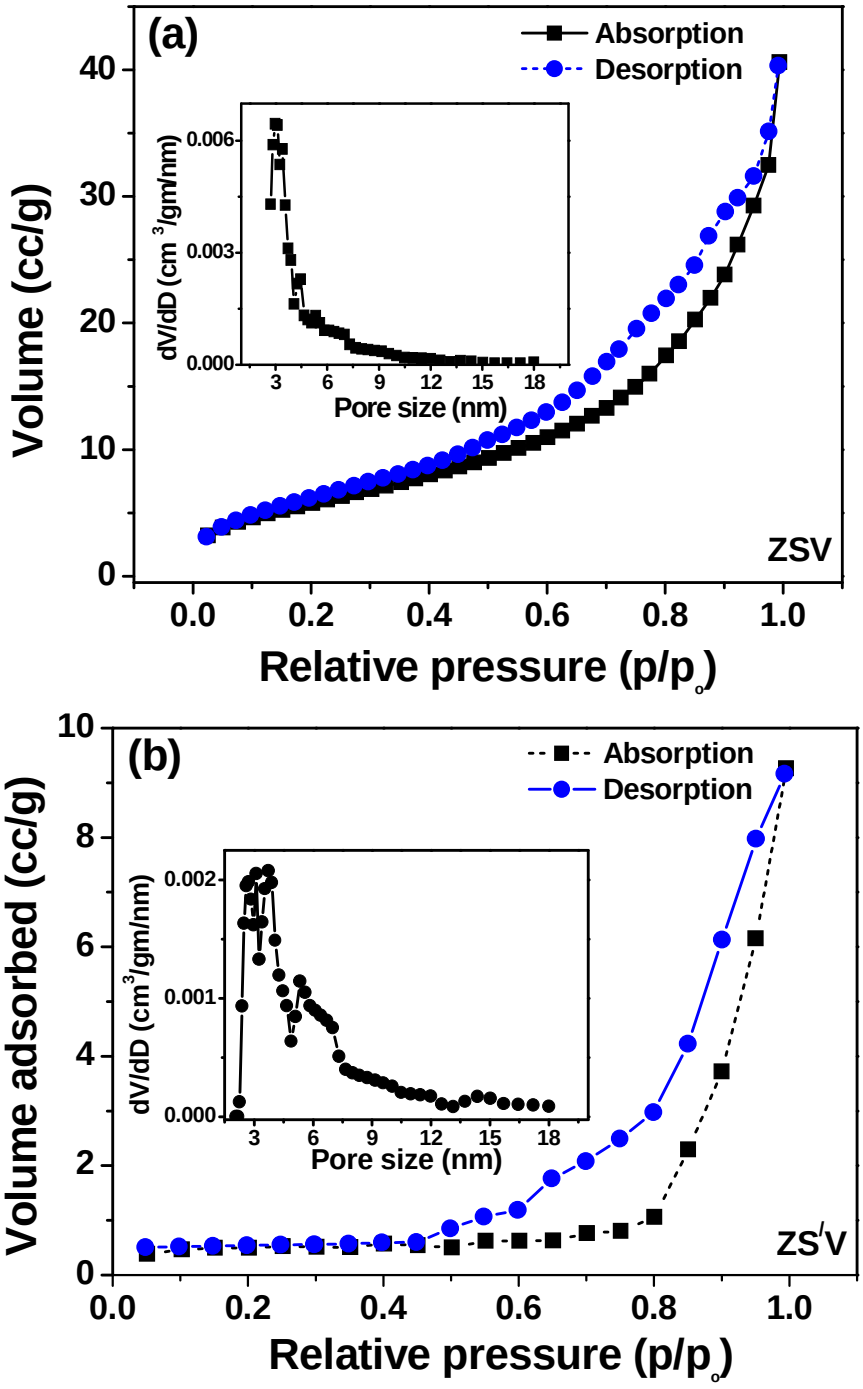

Fig. 7

View Article Online
DOI: 10.1039/C5RA12322D

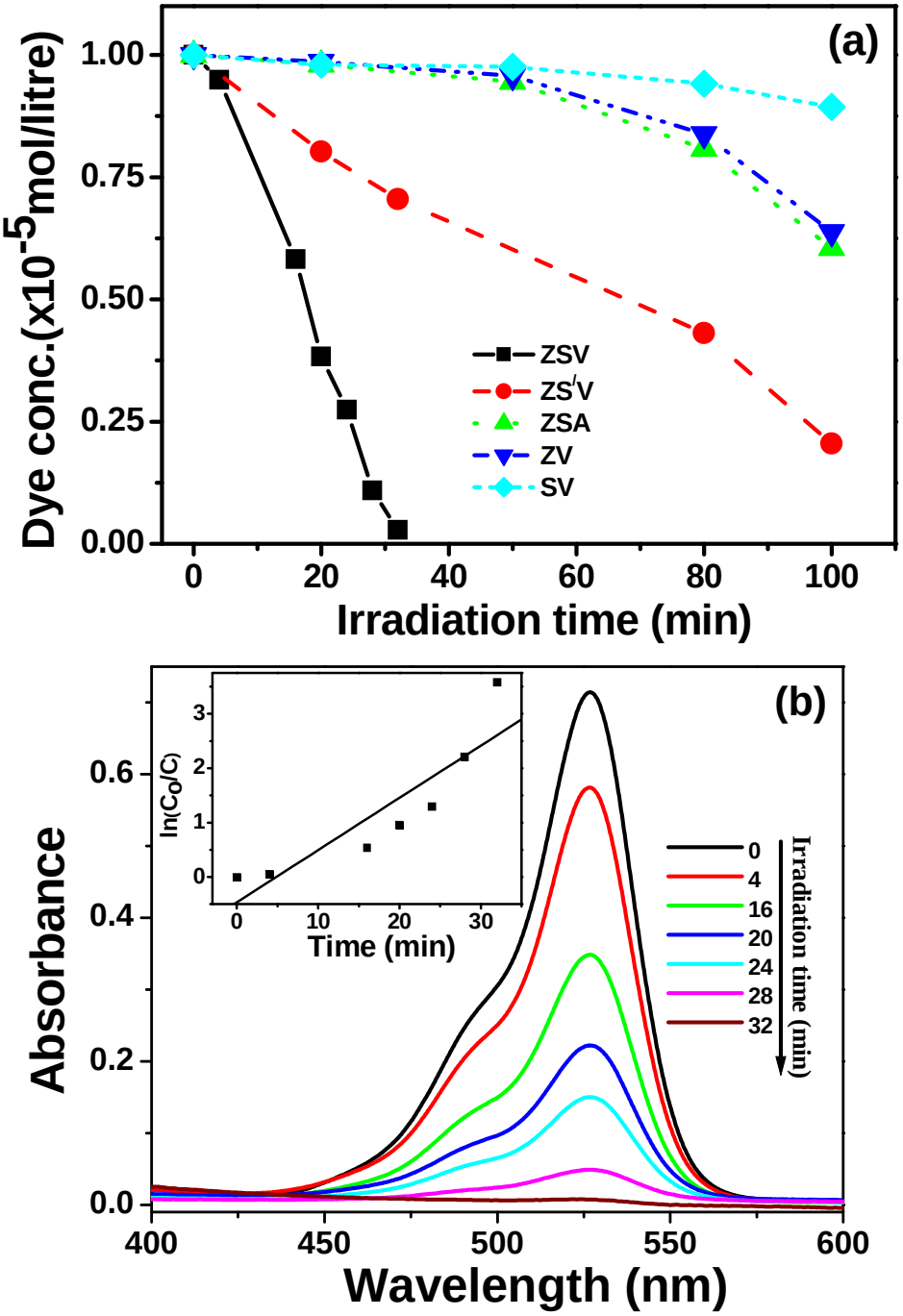

Fig. 8a,b

View Article Online
DOI: 10.1039/C5RA12322D

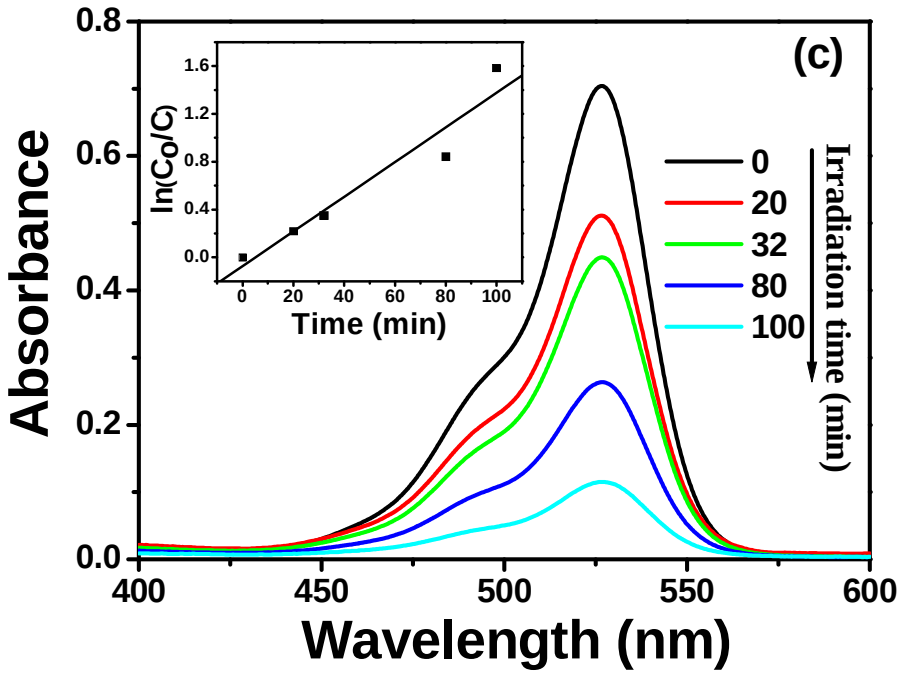

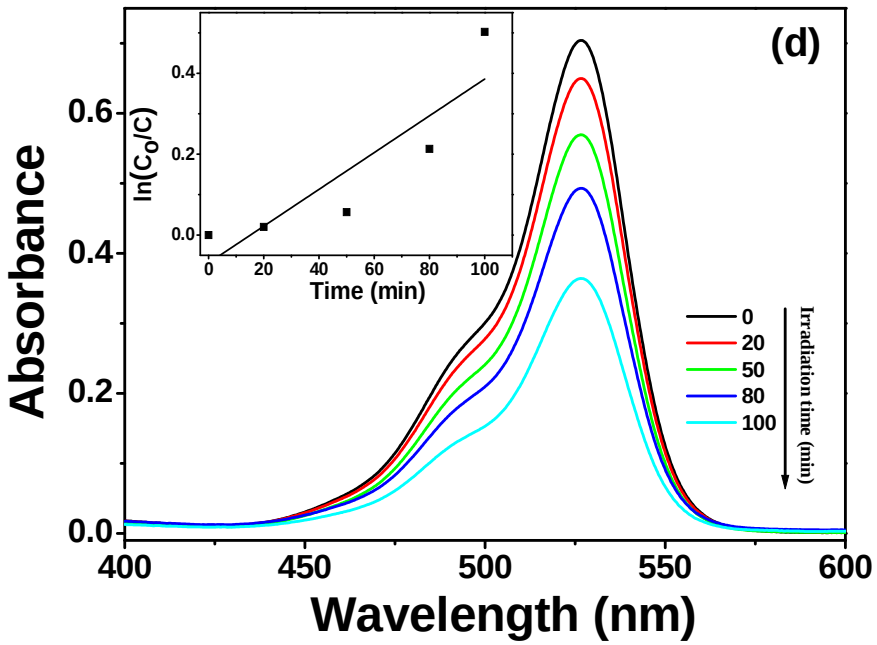

Fig. 8c,d

View Article Online
DOI: 10.1039/C5RA12322D

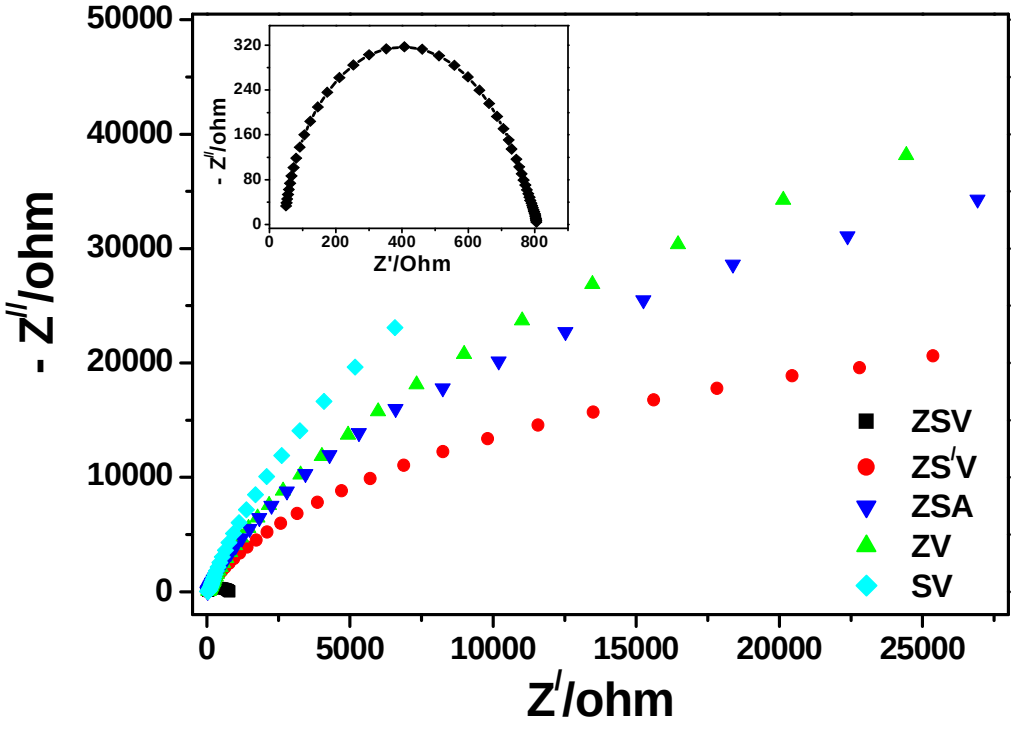

Fig. 9